nature photonics

Supplementary information

https://doi.org/10.1038/s41566-025-01653-w

Space-time-topological events in photonic quantum walks

In the format provided by the authors and unedited

Contents

1 Experimental lattice parameters

Here, we summarise the experimental lattice parameters employed in our experiments. In the following, we denote the coordinates of a spatial and temporal interface as x_0 and t_0, respectively, and define $\beta\left(t,x\right) \equiv \beta_x^t$ with

$$x \leq x_0 : \beta_x^t = \begin{cases} \beta_1^{\mathrm{L}} & \mathrm{mod}\ \ (t,4) = 1 \\ \beta_2^{\mathrm{L}} & \mathrm{mod}\ \ (t,4) = 2 \\ \beta_1^{\mathrm{L}} & \mathrm{mod}\ \ (t,4) = 3 \\ \beta_2^{\mathrm{L}} & \mathrm{mod}\ \ (t,4) = 0 \end{cases}, \quad x > x_0 : \beta_x^t = \begin{cases} \beta_1^{\mathrm{R}} & \mathrm{mod}\ \ (t,4) = 1 \\ \beta_2^{\mathrm{R}} & \mathrm{mod}\ \ (t,4) = 2 \\ \beta_1^{\mathrm{R}} & \mathrm{mod}\ \ (t,4) = 3 \\ \beta_2^{\mathrm{R}} & \mathrm{mod}\ \ (t,4) = 0 \end{cases}, \tag{1}$$

where $\left(\beta_1^{\mathrm{L}}, \beta_2^{\mathrm{L}}\right)$ and $\left(\beta_1^{\mathrm{R}}, \beta_2^{\mathrm{R}}\right)$ denote the parameters at the *left* and *right* from the interface, respectively. For the complex phase modulation, we denote

$$t \leq t_0 : \varphi_{u,x}^t = \begin{cases} \varphi^{\mathrm{B}} & \mathrm{mod}\ \ (t,4) = 1 \\ 0 & \mathrm{mod}\ \ (t,4) = 2 \\ 0 & \mathrm{mod}\ \ (t,4) = 3 \\ -\varphi^{\mathrm{B}} & \mathrm{mod}\ \ (t,4) = 0 \end{cases}, \quad t > t_0 : \varphi_{u,x}^t = \begin{cases} \varphi^{\mathrm{A}} & \mathrm{mod}\ \ (t,4) = 1 \\ 0 & \mathrm{mod}\ \ (t,4) = 2 \\ 0 & \mathrm{mod}\ \ (t,4) = 3 \\ -\varphi^{\mathrm{A}} & \mathrm{mod}\ \ (t,4) = 0 \end{cases}, \tag{2}$$

such that φ^{B} and φ^{A} denote the phase parameter *before* and *after* the temporal interface, respectively. Note, that the phase modulation is distributed anti-symmetrically on the spin-degree of freedom, i.e., $\varphi_{v,x}^t = -\varphi_{u,x}^t$, if not explicitly stated otherwise.

Spatial interface For the spatial interfaces (Fig. 3a), we implemented

$$\left(\beta_1^{\mathrm{L}}, \beta_2^{\mathrm{L}}\right) = (0.75, 1.15)\,, \quad \left(\beta_1^{\mathrm{R}}, \beta_2^{\mathrm{R}}\right) = (1.15, 0.75)\,, \quad \left(\varphi^{\mathrm{B}}, \varphi^{\mathrm{A}}\right) = (0, 0)\,, \tag{3}$$

for the topological case and

$$\left(\beta_1^{\mathrm{L}}, \beta_2^{\mathrm{L}}\right) = (1.15, 0.75)\,, \quad \left(\beta_1^{\mathrm{R}}, \beta_2^{\mathrm{R}}\right) = (1.15, 1.00)\,, \quad \left(\varphi^{\mathrm{B}}, \varphi^{\mathrm{A}}\right) = (0, 0)\,, \tag{4}$$

for the trivial case.

Temporal interface For the temporal interfaces (Fig. 3b), we implemented

$$\left(\beta_1^{\mathrm{L}}, \beta_2^{\mathrm{L}}\right) = (0.79, 0.79)\,, \quad \left(\beta_1^{\mathrm{R}}, \beta_2^{\mathrm{R}}\right) = (0.79, 0.79)\,, \quad \left(\varphi^{\mathrm{B}}, \varphi^{\mathrm{A}}\right) = (-0.10\mathrm{i}, 0.10\mathrm{i})\,, \tag{5}$$

for the topological case and

$$\left(\beta_1^{\mathrm{L}}, \beta_2^{\mathrm{L}}\right) = (0.79, 0.79)\,, \quad \left(\beta_1^{\mathrm{R}}, \beta_2^{\mathrm{R}}\right) = (0.79, 0.79)\,, \quad \left(\varphi^{\mathrm{B}}, \varphi^{\mathrm{A}}\right) = (0.05\mathrm{i}, 0.10\mathrm{i})\,, \tag{6}$$

with $\varphi_{v,x}^t = 0$ for the trivial case to reduce the exponential power growth.

Space-time interface For the space-time interfaces (Fig. 4), we implemented

$$\left(\beta_1^{\mathrm{L}}, \beta_2^{\mathrm{L}}\right) = (0.95, 0.60)\,, \quad \left(\beta_1^{\mathrm{R}}, \beta_2^{\mathrm{R}}\right) = (0.60, 0.95)\,, \quad \left(\varphi^{\mathrm{B}}, \varphi^{\mathrm{A}}\right) = (-0.10\mathrm{i}, 0.10\mathrm{i}) \tag{7}$$

for the topological case (Fig. 4a), and

$$\left(\beta_1^{\mathrm{L}}, \beta_2^{\mathrm{L}}\right) = (0.81, 0.68)\,, \quad \left(\beta_1^{\mathrm{R}}, \beta_2^{\mathrm{R}}\right) = (0.84, 0.73)\,, \quad \left(\varphi^{\mathrm{B}}, \varphi^{\mathrm{A}}\right) = (-0.12\mathrm{i}, -0.08\mathrm{i})\,, \tag{8}$$

with $\varphi_{v,x}^t = 0$ for the trivial one (Fig. 4b).

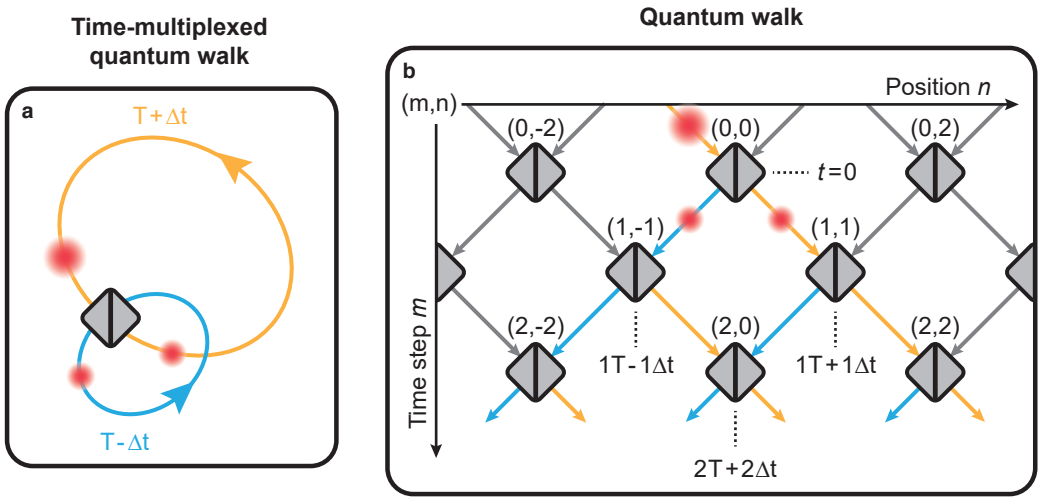

Supplementary Figure 1: Quantum walks through time-multiplexing. a, The propagation of pulses in coupled optical fibre loops is captured by a one-dimensional discrete-time quantum walk, here represented by a photonic mesh lattice of coupled beam splitters. Starting with a single pulse (red-filled circle), it splits up, and the resulting pulses subsequently return to the beam splitter with a relative delay $2\Delta t$. **b**, This temporal separation can be mapped to a spatial separation. At the end of the next circulation, there are four pulses (not shown), but only three possible arrival times. The resulting interplay of relative delays and multipath-interference maps to the (1+1)D beam splitter lattice. The position n and time step m of each pulse is thus encoded in its relative delay $n \cdot \Delta t$ and accumulative roundtrip time $m \cdot T$, respectively.

2 Synthetic dimensions through time-multiplexing

In this section, the mapping of the light propagation of optical pulses in two coupled optical fibre loops[1,2] to the light propagation through a (1+1)D photonic mesh lattice (i.e., the discrete-time quantum walk) is shown (Supplementary Fig. 1).

Importantly, due to the representation of time steps by the accumulative roundtrip delay, unique features of a time dimension (compared to a spatial dimension), such as its unidirectional flow, carry over, hence yielding a genuine synthetic time dimension. In contrast, the synthetic position is related to the *relative* time delays only, thus enabling forwards and backwards coupling of pulses between different positions, forming a synthetic space dimension. Furthermore, also the maximum propagation speed of information is limited: This synthetic speed of light in the (1+1)D photonic mesh lattice is equal to one, i.e., one position step $\Delta n = 1$ per time step $\Delta m = 1$.

Upon including the phase and gain-loss modulations, the pulse dynamics in the photonic mesh lattice is captured by Eq. (1) of the main text, where we have renamed the time step $m \to t$ and position $n \to x$.

3 Quantum walk notation

It is useful to determine the matrix representation of the time-evolution operator U, for instance, to obtain eigenstates and eigenvalues, or for a symmetry analysis. To this end, we introduce the

overall state in Dirac's bra-ket notation as

$$\Psi^t = \sum_n u_x^t \left|x\right\rangle \otimes \left|\leftarrow\right\rangle + v_x^t \left|x\right\rangle \otimes \left|\rightarrow\right\rangle \tag{9}$$

and the evolution equation then read

$$\Psi^{t+1} = U\Psi^t, \quad U = SC \tag{10}$$

with the spin-rotation and spatial shift

$$S = \sum_x \begin{pmatrix} \left|x-1\right\rangle \left\langle x\right| & 0 \\ 0 & \left|x+1\right\rangle \left\langle x\right| \end{pmatrix}, \tag{11}$$

$$C = \sum_x \left|x\right\rangle \left\langle x\right| C_x^t, \tag{12}$$

where we have chosen a spin representation as $\left|\rightarrow\right\rangle = (0,1)^\top$ and $\left|\leftarrow\right\rangle = (1,0)^\top$. Finally, in a lattice with N sites, a straightforward position basis are the N orthogonal unit-vectors, each having only one non-zero entry. In accordance with the evolution equation,

$$\begin{pmatrix} u_{x-1}^{t+1} \\ v_{x+1}^{t+1} \end{pmatrix} = C_x^t \begin{pmatrix} u_x^t \\ v_x^t \end{pmatrix}, \tag{13}$$

the local coin at time step t and position x has the form

$$C_x^t = \begin{pmatrix} \mathrm{e}^{\mathrm{i}\varphi_{u,x-1}^t} & 0 \\ 0 & \mathrm{e}^{\mathrm{i}\varphi_{v,x+1}^t} \end{pmatrix} \begin{pmatrix} \cos\beta_x^t & \mathrm{i}\sin\beta_x^t \\ \mathrm{i}\sin\beta_x^t & \cos\beta_x^t \end{pmatrix} \tag{14}$$

The first matrix describes the beamsplitter with variable beam splitting ratio, β. The second matrix results from augmenting a complex phase $\varphi_{u,v}$ at both outputs.

4 Effective Hamiltonian picture

One can associate a time-independent effective Hamiltonian H to the four-step time evolution operators via

$$U = \mathrm{e}^{-\mathrm{i}H}. \tag{15}$$

An elegant way to obtain H for two-band systems in momentum space is from the time evolution operator in momentum space, $U \in \mathbb{C}^{2\times 2}$ by using the identity

$$\mathrm{e}^{-\mathrm{i}\vartheta(\boldsymbol{n}\cdot\boldsymbol{\sigma})} = \cos(\vartheta)\,\boldsymbol{I}_2 - \mathrm{i}\sin(\vartheta)\,(\boldsymbol{n}\cdot\boldsymbol{\sigma}), \tag{16}$$

and therefore

$$H = \theta\,(\boldsymbol{n}\cdot\boldsymbol{\sigma}), \quad 2\cos\theta = \mathrm{tr}\,(U), \quad \boldsymbol{n} = \frac{\mathrm{i}}{\sin\theta} \begin{pmatrix} U_{12}+U_{21} \\ \mathrm{i}U_{12} - \mathrm{i}U_{21} \\ U_{12} - U_{22} \end{pmatrix}, \tag{17}$$

with $\boldsymbol{\sigma} = (\sigma_x, \sigma_y, \sigma_z)^\top$ and σ_i denoting the Pauli matrices.

5 Band structure and symmetry analysis

Energy bands Upon applying the Bloch ansatz

$$\begin{pmatrix} u_x^t \\ v_x^t \end{pmatrix} = \begin{pmatrix} a \\ b \end{pmatrix} \mathrm{e}^{\mathrm{i}\frac{k}{2}x}, \tag{18}$$

one obtains the time evolution operator in momentum space

$$U(k) = \underbrace{S\Phi(\mathrm{i}g)\,B(\beta_2)}_{\text{Step 4}} \cdot \underbrace{SB(\beta_1)}_{\text{Step 3}} \cdot \underbrace{SB(\beta_2)}_{\text{Step 2}} \cdot \underbrace{S\Phi(-\mathrm{i}g)\,B(\beta_1)}_{\text{Step 1}}, \tag{19}$$

with

$$\begin{aligned} S &= \mathrm{e}^{\mathrm{i}\frac{k}{2}\sigma_3}, \\ B(\beta) &= \mathrm{e}^{\mathrm{i}\beta\sigma_1}, \\ \Phi(\phi) &= \mathrm{e}^{\mathrm{i}\phi\sigma_3}, \end{aligned} \tag{20}$$

denoting the beamsplitting operation B, the complex phase modulation Φ and the subsequent spin-dependent spatial shift S. The mathematical form of these individual operations is typical for discrete-time quantum walks in photonic lattices.[3,4] The quasienergies E can be extracted from the eigenvalues $\mathrm{e}^{-\mathrm{i}E}$ for each k. The model has a four-step temporal periodicity corresponding to four rows of beamsplitters in the photonic lattice. The resulting dispersion relation reads

$$\begin{aligned} \cos(E) = &\cos(2k)\cos^2(\beta_1)\cos^2(\beta_2) - \cos(2\beta_2)\cosh(2g)\sin^2(\beta_1) - \cos^2(\beta_1)\sin^2(\beta_2) \\ &- 4\cos(k)\cos(\beta_1)\cos(\beta_2)\cosh^2(g)\sin(\beta_1)\sin(\beta_2), \end{aligned} \tag{21}$$

giving an analytical form of the energy bands of the system.

Symmetry analysis One directly sees that $E(k)$ is invariant under $k \to -k$ and $E \to -E$, which is in line with the following results. For the symmetry analysis, we apply the unitary transformation

$$U_{\mathrm{sy}} \equiv \mathrm{e}^{\mathrm{i}\frac{\beta_2}{2}\sigma_1} U \mathrm{e}^{-\mathrm{i}\frac{\beta_2}{2}\sigma_1}, \tag{22}$$

to identify the three symmetry relations

$$\begin{aligned} U_{\mathrm{sy}}^* &= U_{\mathrm{sy}}^{-1}, \\ \sigma_2 U_{\mathrm{sy}} \sigma_2 &= U_{\mathrm{sy}}^\dagger, \\ \sigma_3 U_{\mathrm{sy}}(k)\,\sigma_3 &= U_{\mathrm{sy}}^*(-k). \end{aligned} \tag{23}$$

Via $U_{\mathrm{sy}} = \mathrm{e}^{-\mathrm{i}H}$, one can derive the following symmetry relations for the associated effective Hamiltonian H

$$\begin{aligned} H(k) &= H^*(k), \\ \sigma_2 H^\dagger(k)\,\sigma_2 &= -H(k), \\ \sigma_3 H(k)\,\sigma_3 &= -H^*(-k). \end{aligned} \tag{24}$$

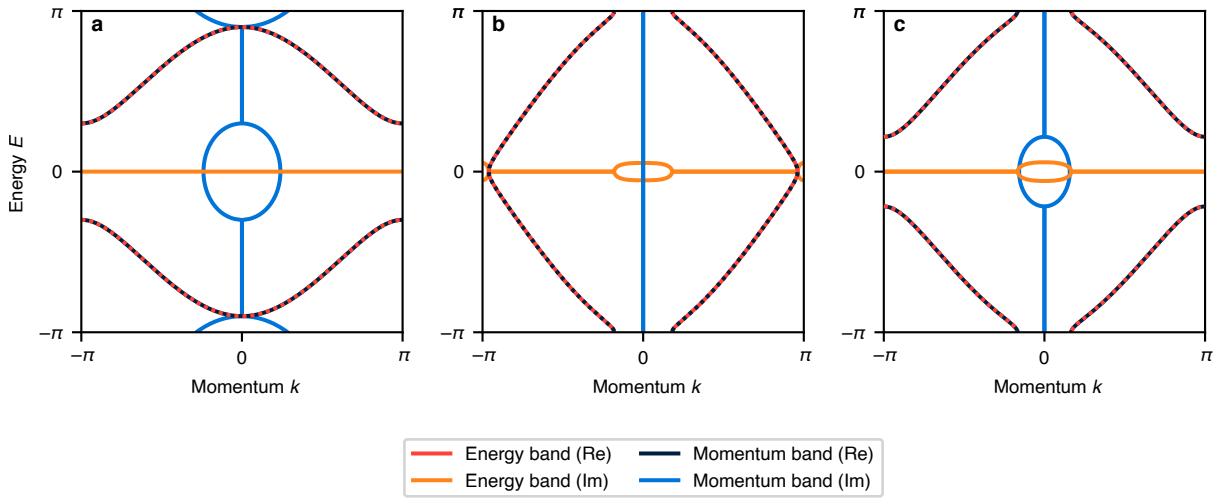

Supplementary Figure 2: Energy and momentum bands. **a**, Energy and momentum bands in the presence of an energy gap. **b**, Energy and momentum bands in the presence of a momentum gap. **c**, Energy and momentum bands in the presence of an energy-momentum gap. The real parts of energy and momentum bands overlap, which is indicated by dotting of the lines.

The first relation implies that H is real and thereby time-reversal symmetric as it commutes with the complex conjugation operator $\mathcal{K}$ and, thus, it is also parity-time symmetric. As a result, all eigenvalues E and eigenstates ψ_E appear in complex conjugated pairs

$$(E, \psi_E) \longleftrightarrow (E^*, \psi_E^*)\,. \tag{25}$$

The second relation is the pseudo-anti Hermiticity. To derive the resulting structure of the spectrum, we denote the left and right eigenstates as $\chi^\dagger$ and ψ, respectively, i.e.,

$$\begin{aligned} H\psi_E &= E\psi_E, \\ H^\dagger \chi_E &= E^* \chi_E. \end{aligned} \tag{26}$$

Thus, the pseudo-anti Hermicity implies that for every right eigenstate ψ_E with quasienergy E there is a correspondingly conjugated eigenstate $\sigma_2\chi_E$ with quasienergy $-E^*$, i.e.,

$$(E, \psi_E) \longleftrightarrow (-E^*, \sigma_2\chi_E) \tag{27}$$

and it therefore can be regarded as a non-Hermitian version of chiral symmetry. The third symmetry relation represents a type of inversion symmetry, which implies conjugated pairing of eigenstates with inverted momentum k, i.e.,

$$(E(k), \psi_E(k)) \longleftrightarrow (-E^*(-k), \sigma_3\psi_E^*(-k))\,. \tag{28}$$

We note here, that these symmetries preclude a spectral winding. Hence, this model does not exhibit the non-Hermitian skin effect.

Momentum bands This subsection concerns itself with the definition and calculation of momentum bands. To this end, it is instructive to briefly recapitulate the intuitive definition of an energy

band: It is the function, that given real momentum $k \in \mathbb{R}$ will assign an energy $E \in \mathbb{C}$ to it. Conversely, a momentum band is the function that given a real energy $E \in \mathbb{R}$ will assign a momentum $k \in \mathbb{C}$ to it. While the procedure to derive momentum bands is straightforward, as they are immediately given by the eigenvalue problem for the Hamiltonian

$$E(k) = \operatorname{eig} H(k), \tag{29}$$

it is generally less clear how to derive momentum bands.

First of all, it is helpful to note that energy and momentum bands coincide where the energy bands and thus the pair of energy and momentum are real, as shown in Supplementary Figure 2. However, this problem becomes less clear when there is an energy gap: Here, the eigenvalue problem in Eq. (29) may be inverted to find a (non-real) momentum which yields a real energy eigenvalue and hence a point on the momentum band. In our case, this inversion was performed numerically. This solution for the momentum is imaginary, as can be seen in Supplementary Figure 2a and 2b. This intuitively makes sense, as the solutions in the energy gap are evanescent waves that decay in space. Thus, an energy gap occurs when the momentum bands turn imaginary and conversely, a momentum gap occurs when the energy bands turn imaginary. We note here that, while we did not originally choose this approach, alternatively, momentum bands can also be determined by calculating the transfer matrix and solving its eigenvalue problem instead, as discussed in Section 8.

Lastly, with a wider view, we point out that the symmetries of our model constrain it to possess energy and momentum bands which are either purely real or imaginary (or complex with a constant real part of $\pm\pi$), leading to the aforementioned correspondence between real energy and momentum bands. However, this is not the case in models with complex bands which are not purely real or imaginary: Here, the energy and momentum bands obey no such correspondence, hinting at the intriguing possibility of models where the complex energy and momentum band structure may look entirely different, potentially opening up a vastly bigger parameter space for the engineering of energy-momentum band structures.

6 Calculation of topological invariants

This section describes the calculation of the topological invariants for this work, i.e., of a space-topological, a time-topological and a spacetime-topological invariant.

Space-topological invariant We begin with the known formulation of space-topological invariants. These invariants predict the existence of edge states at spatial interfaces. In (1+1)D systems like the one considered here, a commonly used invariant is the winding number[5]. It is well-defined only if an energy gap is open and may be calculated from the global accumulation of phase of the eigenstates $\psi_E(k)$ evolving along the energy bands[6]

$$w_{\text{space}} = \frac{\mathrm{i}}{2\pi} \sum_E \int_{k=-\pi}^{k=\pi} \psi_E^\dagger(k) \frac{\partial}{\partial k} \psi_E(k) \, \mathrm{d}k, \tag{30}$$

where the sum runs over all energy bands. The topological invariant predicting if a spatial interface is topological, i.e., whether it hosts topological states, is the difference of winding numbers in the

half-spaces A and B separated by the interface

$$n_{\text{space}} = w^{\text{A}}_{\text{space}} - w^{\text{B}}_{\text{space}}. \tag{31}$$

If $n_{\text{space}} \neq 0$, the spatial interface is (space-)topological, otherwise it is trivial and does not host a topological state. This relation is also known as the bulk-boundary correspondence[5]. The fact that this invariant needs to be quantised derives from the symmetry shown in Eq. (28), which places restrictions on the precise form of the eigenvectors that guarantee that the winding number must be an integer.

Time-topological invariant Intuitively, as for space the energy gap determines the topology, for time it appears likely to be the momentum gap, as energy determines the temporal features of the eigenstates whereas momentum determines their spatial features making their roles in space and time topology analogous. Following this line of reasoning, we see that the resulting novel time-topological invariants correctly predict the emergence of time-topological states, and these invariants take the elegant form of a topological winding along momentum bands, making them appear as the natural way to capture these topological phenomena. Attempting to use a traditional (complex) energy-band approach instead, would, thus, lead to complicated expressions with no such direct interpretation as winding numbers, which in effect would also amount to indirectly calculating momentum bands.

The momentum gap which separates momentum bands is relevant to the calculation of the invariant. As described in more detail in Section 5, whereas energy bands are defined by a set of energies E assigned to each real momentum k, momentum bands assign a momentum k to each real energy E. A momentum gap is a range of momenta where the real part of the energy is 0 or $\pm\pi$ and its imaginary part is nonzero, i.e., where the solutions grow or decay exponentially. Note, that a similar definition is also possible for energy gaps, where it is the momentum that acquires an imaginary part in the gap. However, as the band structure of systems is often calculated from the Hamiltonian by assuming real momenta and finding its eigenvalues, in such calculations energy gaps commonly appear as ranges of energy where no eigenvalues are found.

Based on this, we have found that along momentum bands too the eigenstates of the system may accumulate a global phase. Hence, the time-topological winding number may be defined as

$$w_{\text{time}} = \frac{\mathrm{i}}{2\pi} \sum_k \int_{E=-\pi}^{E=\pi} \psi_k^\dagger(E) \frac{\partial}{\partial E} \psi_k(E) \, \mathrm{d}E, \tag{32}$$

where the sum runs over all momentum bands. At a temporal interface, the topological invariant predicting whether the interface is time-topological, is then defined as

$$n_{\text{time}} = w^{\text{A}}_{\text{time}} - w^{\text{B}}_{\text{time}}, \tag{33}$$

where A and B denote the two half-"spaces" before and after the interface in time. This quantity must be an integer, as the form of the eigenvectors due to the symmetry in Eq. (28) mandates a quantisation. When the time-topological invariant n_{time} is nonzero, a time-topological state will occur at the temporal interface. Otherwise, when $n_{\text{time}} = 0$, no such state appears. These predictions match with the experimental observations made in Fig. 3b.

Spacetime-topological invariant For the purpose of defining a spacetime-topological invariant which accurately predicts spacetime-topological events, it is necessary to consider energy-momentum gapped systems. For the calculation of the invariant, it is important to note that the simultaneous presence of energy and momentum gaps precludes fully real energy or momentum bands. Furthermore, the aforementioned presence of an energy gap means that the momentum bands cannot be derived from the Hamiltonian as straightforwardly. Instead, they can be found by solving the inverse problem of determining the complex momenta for which the eigenvalues of the Hamiltonian remain real. For these complex momenta, the eigenstates of the system may then be determined.

Integrating the energy-gapped momentum band as well as the momentum-gapped energy band, i.e., an energy-momentum surface integral of the Floquet-Brillouin zone, then simplifies to an elegant expression for the spacetime-topological invariant as

$$n_{\text{spacetime}} = n_{\text{space}} n_{\text{time}}. \tag{34}$$

This spacetime-topological invariant predicts whether the event is topological, i.e., whether there is spatiotemporal localisation due to topology at a unique point in spacetime. If it is nonzero, the event is spacetime-topological, otherwise it is trivial and the characteristic exponential localisation of topological states does not occur. The invariant correctly predicts when our system is spacetime-topological or spacetime-trivial, matching our experimental observations shown in Fig. 4a and Fig. 4b, respectively.

7 Temporal bulk-boundary correspondence

As a first step, we recall, that the temporal evolution rule for quantum walks reads

$$\Psi^{t+1} = U\Psi^{t}. \tag{35}$$

Nevertheless, this set of equations may always be rearranged into a spatial evolution rule instead, which is a common procedure leading to the transfer matrix formalism

$$\Phi^{x+1} = T\Phi^{x}, \tag{36}$$

where T is the transfer matrix. Note, that while at first glance both evolution rules are visually similar, only time evolution respects causality. In the transfer matrix formalism, the system evolves along the spatial direction, which requires knowledge about the future and past of the system as initial condition, violating causality. Conversely, time evolution requires knowledge of the system everywhere in space but only at one time, which preserves causality. However, for our purpose of topological physics, we are looking to make statements about eigenstates of the system, which are fully determined in both space and time irrespective of any initial condition. It is well known, that based on the Floquet-Bloch eigenstates of $U(k)$, one can calculate (space-)topological invariants, which then allow to apply the bulk-boundary correspondence[5,7,8]. This conventional bulk-boundary correspondence states, that if two quantum walks described by time evolution operators U^{A} and U^{B} are coupled at the position x_0, such that

$$U = \begin{cases} U^{\mathrm{A}} & x \leq x_0 \\ U^{\mathrm{B}} & x > x_0 \end{cases}, \tag{37}$$

a topological state is proven to emerge in the common energy gap region of U^{A} and U^{B} at $E = 0$, which is exponentially localised at x_0, if and only if U^{A} and U^{B} differ in their respective topological invariant. The emergence of such a state can then be verified by evaluating the spectrum (a protected state can be found at $E = 0$) or time evolution of U (a protected localised state can be excited at x_0), now in real space due to the interface.

Now, consider a system with a temporal interface at $t = t_0$, such that

$$T = \begin{cases} T^{\mathrm{A}} & t \leq t_0 \\ T^{\mathrm{B}} & t > t_0 \end{cases}. \tag{38}$$

Comparing Eqs. (35) and (36) as well as Eqs. (37) and (38), it is evident that when exchanging U and T, these equations become mathematically equivalent as well as physically equivalent up to an exchange of time and space. Hence, it follows from the conventional bulk-boundary correspondence as detailed above, that a time-topological edge state localised at a temporal interface should appear if the system is evolved in time with a time evolution operator that is the transfer matrix of a system with a space-topological edge state. As a remarkable result, such a topological system exhibits a momentum gap instead of an energy gap, and its momentum gap is associated with a time-topological invariant, which is based on the geometric phase accumulated when tracing along the momentum bands, as detailed in Section 5.

8 Transfer matrix

The original model has a 4×2 Floquet-Bloch unit cell covering four beamsplitters with complex phase modulations at the outputs (Fig. 2b). The associated time evolution operator updates in time steps $t \to t + 1$. To obtain the transfer matrix, we rewrite the equations as spatial step updates, i.e., $x \to x + 1$. The resulting transfer matrix in Floquet space reads

$$T = \begin{pmatrix} 0 & M_2^{\uparrow} \mathrm{e}^{\mathrm{i}\frac{k}{4}} & 0 & M_4^{\uparrow} \mathrm{e}^{-\mathrm{i}\frac{k}{4}} \\ M_1^{\downarrow} \mathrm{e}^{-\mathrm{i}\frac{k}{4}} & 0 & M_3^{\uparrow} \mathrm{e}^{\mathrm{i}\frac{k}{4}} & 0 \\ 0 & M_2^{\downarrow} \mathrm{e}^{-\mathrm{i}\frac{k}{4}} & 0 & M_4^{\uparrow} \mathrm{e}^{\mathrm{i}\frac{k}{4}} \\ M_1^{\uparrow} \mathrm{e}^{\mathrm{i}\frac{k}{4}} & 0 & M_3^{\downarrow} \mathrm{e}^{-\mathrm{i}\frac{k}{4}} & 0 \end{pmatrix}, \tag{39}$$

where

$$M_j^{\uparrow} = \begin{pmatrix} 1 & 0 \\ 0 & 0 \end{pmatrix} M_j, \quad M_j^{\downarrow} = \begin{pmatrix} 0 & 0 \\ 0 & 1 \end{pmatrix} M_j, \tag{40}$$

and

$$
\begin{aligned}
M_1 &= \begin{pmatrix} \mathrm{e}^{-g}\sec(\beta_2) & \mathrm{i}\mathrm{e}^{-2g}\tan(\beta_2) \\ -\mathrm{i}\tan(\beta_2) & \mathrm{e}^{-g}\sec(\beta_2) \end{pmatrix}, \\
M_2 &= \begin{pmatrix} \sec(\beta_1) & \mathrm{i}\tan(\beta_1) \\ -\mathrm{i}\tan(\beta_1) & \sec(\beta_1) \end{pmatrix}, \\
M_3 &= \begin{pmatrix} \sec(\beta_2) & \mathrm{i}\tan(\beta_2) \\ -\mathrm{i}\tan(\beta_2) & \sec(\beta_2) \end{pmatrix}, \\
M_4 &= \begin{pmatrix} \mathrm{e}^{g}\sec(\beta_1) & \mathrm{i}\mathrm{e}^{2g}\tan(\beta_1) \\ -\mathrm{i}\tan(\beta_1) & \mathrm{e}^{g}\sec(\beta_1) \end{pmatrix}.
\end{aligned}
\tag{41}
$$

Solving the eigenvalue problem

$$
\vec{\psi}\mathrm{e}^{\mathrm{i}k} = T^2\vec{\psi}, \tag{42}
$$

yields the momentum bands $k(E)$ of the original model.

We would also like to make a brief comment on the implications of the fact that momentum bands and thus temporal topological features appear to be most naturally described in terms of the transfer matrix and not the time evolution operator: This fact leads to a lack of separability (as these two operators are inextricably but non-trivially linked) where for example spatiotemporal topological features that arise from the energy-momentum gap (i.e., a combined spectral feature of time evolution operator and transfer matrix) may not simply be split into a superposition of spatial and temporal features.

9 Dynamics of a temporal interface

Examining dynamics in the traditional way, i.e. thinking locally in time, a system which experiences a temporal interface at $t = t_0$ where the effective non-Hermitian Hamiltonian is quenched from $H^{\mathrm{B}} \to H^{\mathrm{A}}$ cannot have knowledge of this change for $t < t_0$ as a result of causality and will evolve according to H^{B}. The superscript B and A denote the Hamiltonian before and after the time interface, respectively. Following the interface, the system then evolves according to H^{A}. The time evolution operator of the temporal interface is given by,

$$
U(t,0) = \begin{cases} \exp\left(-\mathrm{i}H^{\mathrm{B}}t\right) & \text{for } t_0 > t, \\ \exp\left(-\mathrm{i}H^{\mathrm{A}}(t-t_0)\right)\exp\left(-\mathrm{i}H^{\mathrm{B}}t_0\right) & \text{for } t > t_0. \end{cases} \tag{43}
$$

If the system is initially excited into some state $|\psi_0\rangle$, then at the point of the temporal interface the system will be in the state $|\psi(t=t_0)\rangle = \exp\left(-\mathrm{i}H^{\mathrm{B}}t_0\right)|\psi_0\rangle$. Note that this state depends on the choice of H^{B}, t_0, and $|\psi_0\rangle$. After the interface, the state is evolved according to H^{A}; this can be calculated explicitly by using the non-Hermitian counterpart of the canonical eigenstate expansion. This is facilitated by the biorthogonal completeness relation $\mathbb{1} = \sum_E |\psi_E\rangle\langle\chi_E| \,/\, \langle\chi_E|\,\psi_E\rangle$ composed of left and right eigenvectors $|\chi_E\rangle$ and $|\chi_E\rangle$ at energy E, respectively, which assumes that $\langle\chi_E|\,\psi_E\rangle \neq 0 \;\forall\; E$ and H is non-degenerate[9]. This produces the following general expression for dynamics after the interface,

$$
|\psi(t>t_0)\rangle = \sum_E \frac{\langle\chi_E^{\mathrm{A}}|\,\psi(t=t_0)\rangle}{\langle\chi_E^{\mathrm{A}}|\,\psi_E^{\mathrm{A}}\rangle} e^{-\mathrm{i}E^{\mathrm{A}}(t-t_0)}\left|\psi_E^{\mathrm{A}}\right\rangle, \tag{44}
$$

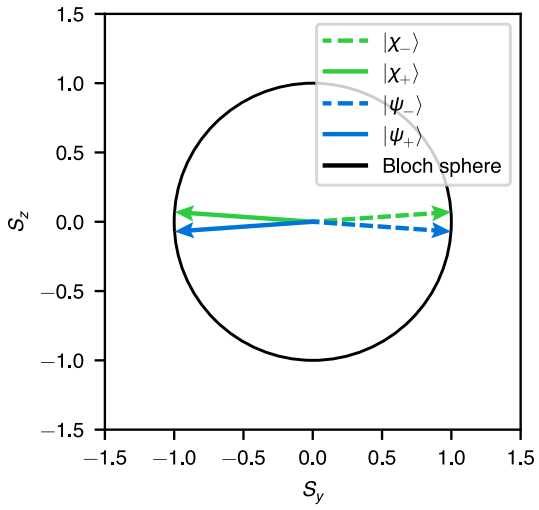

Supplementary Figure 3: Cross configuration of $k = 0$ left and right eigenstates. The quantum walk parameters used are $\phi = 0.1\mathrm{i}$, $\beta_1 = \beta_2 = \pi/4$ and $S_{y(z)}$ is defined as $\langle a| \sigma_{y(z)} |a\rangle$ for arbitrary state $|a\rangle$. The symmetries of the model constrain eigenstates into a cross configuration within the $y - z$ plane of the Bloch sphere.

where the superscript A denotes being defined with respect to H^{A}, and E^{A} refers to the energy eigenvalues of H^{A} which are in general complex. The intensity profile around the temporal interface is then determined by the overlaps,

$$c_n = \frac{\langle \chi_E^{\mathrm{A}}|\ \psi(t = t_0)\rangle}{\langle \chi_E^{\mathrm{A}}|\ \psi_E^{\mathrm{A}}\rangle}, \tag{45}$$

which is the only dynamics-influencing quantity in this expansion depending on both H^{B} and H^{A}.

10 Intensity profile of time-topological edge states

To determine the nature of the temporal edge state located in the momentum gap about $k = 0$, we examine the relevant overlaps. We note that quasi energies in this gap take the form $E_\pm(k) = \pi \pm \mathrm{i}\gamma(k)$, $\gamma(k) \in \mathbb{R}$. Here E_+ induces dynamics with exponential growth in the amplitude and with exponential decay for E_-. In terms of notation, the subscripts in this section indicate whether an eigenmode is growing $(+)$ or decaying $(-)$. As in the previous section, the superscripts B and A indicate whether an object is referring to the system before or after the time interface, respectively. Lastly, left eigenvectors are always denoted by the Greek letter χ and right eigenvectors by the letter ψ, in keeping with the notation introduced by Brody[9]. Hence, the left and right eigenvectors corresponding to $E_\pm$ are denoted by $|\chi_\pm(k)\rangle$ and $|\psi_\pm(k)\rangle$, respectively. Supposing our initial excitation of the system $|\psi_0\rangle \in \mathrm{Span}\left[\left|\psi_\pm^{\mathrm{B}}(k = 0)\right\rangle\right]$, then because k remains a good quantum number, the state of the system will remain in the $k = 0$ subspace. Hence, in the following we will drop the argument for readability and denote $|\chi_\pm(k = 0)\rangle, |\psi_\pm(k = 0)\rangle$ as $|\chi_\pm\rangle, |\psi_\pm\rangle$ and $\gamma(k = 0)$ as γ_0. If $|\psi_0\rangle = \left|\psi_+^{\mathrm{B}}\right\rangle$, then after the temporal interface the state of the system will be given by,

$$\frac{|\psi(t > t_0)\rangle}{\sqrt{I(t = t_0)}} = e^{-\mathrm{i}\pi(t-t_0)} \left(c_+ e^{\gamma_0(t-t_0)} \left|\psi_+^{\mathrm{A}}\right\rangle + c_- e^{-\gamma_0(t-t_0)} \left|\psi_-^{\mathrm{A}}\right\rangle\right), \tag{46}$$

where $I(t=t_0) = \langle\psi(t=t_0)|\,\psi(t=t_0)\rangle$ refers to the intensity observed at $t=t_0$. The biorthogonal overlap coefficients for the eigenstates before and after the interface follow from Eq. (45) as

$$c_\pm = \frac{\left\langle \chi_\pm^{\mathrm{A}}\right|\,\psi_+^{\mathrm{B}}\rangle}{\left\langle \chi_\pm^{\mathrm{A}}\right|\,\psi_\pm^{\mathrm{A}}\rangle}. \tag{47}$$

The observed intensity for $t > t_0$ under these assumptions is then given by,

$$\frac{I(t>t_0)}{I(t=t_0)} = |c_+|^2 e^{2\gamma_0(t-t_0)} + |c_-|^2 e^{-2\gamma_0(t-t_0)} + (c_+)^* c_- \left\langle \psi_+^{\mathrm{A}}\right|\,\psi_-^{\mathrm{A}}\rangle + \text{c.c.}\ . \tag{48}$$

Computing the time derivative immediately after the quench gives

$$\frac{d}{dt}\tilde{I}(t)\big|_{t=t_0^+} = 2\gamma_0\left(|c_+|^2 - |c_-|^2\right), \tag{49}$$

where $\tilde{I}(t)$ refers to the intensity normalised by the intensity at $t=t_0$. The relative magnitude of the overlaps $c_\pm$ determines whether we see immediate increase or decrease as also captured by the time-topological invariant. Across a temporal topological interface, if the system is initialised in the growing eigenstate $\left|\psi_+^{\mathrm{B}}\right\rangle$ as was assumed in the above analysis, the overlap coefficient of growing states before and after the interface c_+ is non-vanishing in general owing to the non-orthogonality property of the left and right eigenvector sets of a non-Hermitian operator. This naturally produces a time t_g beyond which the intensity profile begins to increase once again. From Eq. (48) it follows that,

$$t_g = t_0 + \frac{1}{2\gamma_0}\ln\left(\frac{|c_-|}{|c_+|}\right), \quad \text{for } |c_-| > |c_+|. \tag{50}$$

Examining the symmetries of the model identified in Section 5 leads to the following relationships between growing and decaying left and right eigenvectors: $|\chi_\pm\rangle = \mathcal{K}\,|\chi_\mp\rangle$, $|\psi_\pm\rangle = \mathcal{K}\,|\psi_\mp\rangle$, $|\chi_\pm\rangle = e^{\mathrm{i}\delta_\pm}\sigma_2\,|\psi_\pm\rangle$, $|\psi_\pm\rangle = e^{\mathrm{i}\phi_\pm}\sigma_3\mathcal{K}\,|\psi_\pm\rangle$. Here $\mathcal{K}$ denotes complex conjugation, $e^{\mathrm{i}\delta_\pm}, e^{\mathrm{i}\phi_\pm}$ are phases undetermined by the symmetry. Central to these relationships is the result $-E_\pm^*(k=0) = E_\pm(k=0) \bmod 2\pi$. The final relationship implies that left and right eigenvectors are constrained to the $y-z$ plane of the Bloch sphere, whereby the operations $\mathcal{K}$ and σ_2 have the geometric action of reflection in the z and y axis respectively. This then leads to a *cross* configuration of left and right eigenvectors as illustrated in Supplementary Fig. 3. We may therefore parameterise the temporal edge state as

$$|\psi(t)\rangle = \left|\psi_{\theta(t)}\right\rangle = \cos\left(\frac{\theta(t)}{2}\right)|0\rangle + \mathrm{i}\sin\left(\frac{\theta(t)}{2}\right)|1\rangle\,,\ \theta\in[-\pi,\pi]. \tag{51}$$

Here θ is the polar angle in the $y-z$ plane relative to the z axis. Substitution into Eq. (48) yields,

$$\begin{aligned}\tilde{I}(t>t_0) =& \frac{\cos^2\left(\frac{\alpha-\theta_{t=t_0}}{2}\right)\mathrm{e}^{2\gamma_0(t-t_0)} + \cos^2\left(\frac{\alpha+\theta_{t=t_0}}{2}\right)\mathrm{e}^{-2\gamma_0(t-t_0)}}{\sin^2(\alpha)} \\ &- \frac{2\cos\left(\frac{\alpha-\theta_{t=t_0}}{2}\right)\cos\left(\frac{\alpha+\theta_{t=t_0}}{2}\right)\cos(\alpha)}{\sin^2(\alpha)},\end{aligned} \tag{52}$$

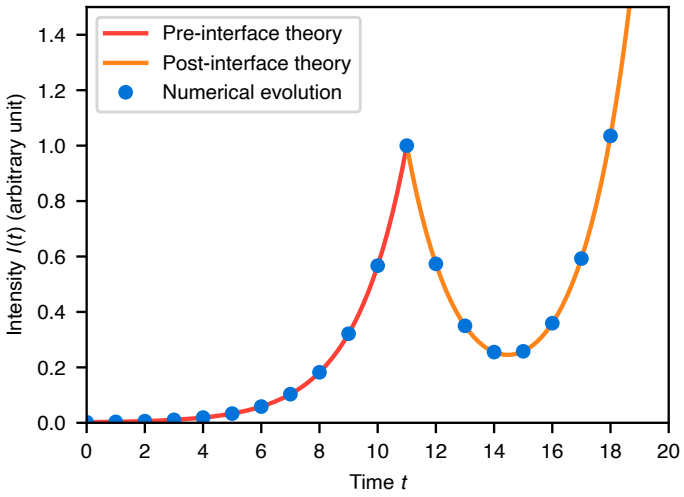

Supplementary Figure 4: Comparison of numerical and analytic intensity profiles of a temporal edge state. Numerical evolution is performed with a spatially periodic lattice of 50 sites where the system is initialised uniformly in the growing eigenstate $\left|\psi_{+}^{\mathrm{B}}\right\rangle$. Pre- and post-temporal interface theory curves are plotted with reference to Eqs. (48) and (52) to which we observe excellent agreement with the numerical evolution. The temporal interface parameters used are $\phi^{\mathrm{B}} = -0.2\mathrm{i}$, $\phi^{\mathrm{A}} = 0.2\mathrm{i}$, $\beta_1 = \beta_2 = \pi/4$ which gives $\alpha \approx -1.43$ as defined with reference to Eq. (52).

where $\theta_{t=t_0}$ corresponds to the angle of the state relative to the z axis at $t = t_0$ and α is defined by $\left|\chi_{+}^{\mathrm{A}}\right\rangle = |\psi_\alpha\rangle$. In this derivation, we made use of the symmetries and the result $\langle\psi_{\theta_1}|\,\psi_{\theta_2}\rangle = \cos\left(\frac{\theta_1-\theta_2}{2}\right)$.

We note that when the state at the temporal interface is orthogonal to the growing left eigenstate after the interface $\left|\chi_{+}^{\mathrm{A}}\right\rangle$, corresponding to the condition $\theta - \alpha = \pm\pi$, the t independent term of Eq. (52) vanishes and $c_+ = 0, c_- = 1$ as expected. For sufficiently large $|\phi|$ either side of the temporal interface, the following approximation $\theta_{t=t_0} \approx -\alpha$ so that $\left|\psi_{\theta_{t=t_0}}\right\rangle \approx \left|\chi_{-}^{\mathrm{A}}\right\rangle$ has been verified numerically. This then gives

$$\tilde{I}(t > t_0) = \cot^2(\alpha)\left(\mathrm{e}^{2\gamma_0(t-t_0)} - 2\right) + \csc^2(\alpha)\,\mathrm{e}^{-2\gamma_0(t-t_0)} \tag{53}$$

for the normalised intensity after the time interface.

We remark that it is in fact possible to rigorously relate the topology of the system to the overlap between growing and decaying modes as we discussed it here. This points toward an alternative approach for proving a bulk-boundary correspondence, which is the subject of further work.

References

1. Yuan, L., Lin, Q., Xiao, M. & Fan, S. Synthetic dimension in photonics. *Optica* **5,** 1396–1405 (2018).
2. Ozawa, T. & Price, H. M. Topological quantum matter in synthetic dimensions. *Nature Reviews Physics* **1,** 349–357 (2019).
3. Xiao, L. *et al.* Observation of topological edge states in parity–time-symmetric quantum walks. *Nature Physics* **13,** 1117–1123 (2017).
4. Mochizuki, K., Kim, D. & Obuse, H. Explicit definition of PT symmetry for nonunitary quantum walks with gain and loss. *Physical Review A* **93,** 062116 (2016).
5. Asbóth, J. K., Oroszlány, L. & Pályi, A. *A Short Course on Topological Insulators* (Springer International Publishing, Cham, 2016).
6. Xue, P., Qiu, X., Wang, K., Sanders, B. C. & Yi, W. Observation of dark edge states in parity-time-symmetric quantum dynamics. *National Science Review* **10,** nwad005 (2023).
7. Cedzich, C. *et al.* Bulk-edge correspondence of one-dimensional quantum walks. *Journal of Physics A: Mathematical and Theoretical* **49,** 21LT01 (2016).
8. Tanaka, Y. A constructive approach to topological invariants for one-dimensional strictly local operators. *Journal of Mathematical Analysis and Applications* **500,** 125072 (2021).
9. Brody, D. C. Biorthogonal quantum mechanics. *Journal of Physics A: Mathematical and Theoretical* **47,** 035305 (2013).